Modeling and measurement of dielectric anisotropy in materials manufactured via fused filament fabrication processes

Hehenberger, Simon P.; Caizzone, Stefano; Yarovoy, Alexander

DOI
10.1016/j.materresbull.2024.112938

Publication date
2024

Document Version
Final published version

Published in
Materials Research Bulletin

Materials Research Bulletin 179 (2024) 112938

Contents lists available at ScienceDirect

Materials Research Bulletin

journal homepage: www.elsevier.com/locate/matresbu

Modeling and measurement of dielectric anisotropy in materials manufactured via fused filament fabrication processes

Simon P. Hehenberger [*,a,b], Stefano Caizzone [a], Alexander Yarovoy [b]

[a] Institute for Communication and Navigation, German Aerospace Center, Wessling, Germany
[b] Department of Microwave Sensing, Signals and Systems, Technische Universiteit Delft, Delft, the Netherlands

ARTICLE INFO

Keywords:
Additive manufacturing
Dielectric anisotropy
Microwave material characterization
Fused filament fabrication
Modeling

ABSTRACT

Additive manufacturing (AM) is increasingly recognized as an enabling technology for novel devices with increased functionality and bandwidth for microwave applications. However, due to the layer-by-layer build approach employed by most AM techniques, internal patterns are introduced to printed materials, which cause an effective anisotropy in their material parameters. An electrostatic model inspired by parallel plate capacitors, describing the dielectric anisotropy of materials manufactured with fused filament fabrication (FFF) AM techniques is proposed in this work. The accuracy of the model's predictions about the permittivity tensor of printed materials is investigated via numerical simulations. Furthermore, permittivity tensor measurements are carried out for samples printed with various materials and print settings. Measurement data is fitted to the model via a least squares approach, and excellent agreement is observed. Novel conclusions about the impact of material and print parameters on the effective permittivity of additively manufactured materials, improving the accuracy in modeling and designing additively manufactured microwave devices are drawn.

1. Introduction

Additive manufacturing (AM) is increasingly recognized as an enabling technology for novel microwave devices with increased functionality and bandwidth. While traditional subtractive manufacturing methods are well suited to process surfaces and achieve unparalleled tolerances, they cannot create intricate geometries throughout the volume of some material. AM techniques are the key to manufacturing volumetric inhomogeneous and anisotropic devices, enabling graded index (GRIN) design approaches and complex metamaterials, impossible to realize with traditionally employed subtractive manufacturing methods. Researchers in the RF, microwave, and mmWave communities have so far exploited the additional degrees of freedom offered by AM in several ways to overcome limitations posed by traditional manufacturing methods [1,2]. Fused filament fabrication (FFF) is especially attractive among the various AM processes due to its capability of producing complex multi-material parts with readily available and inexpensive machines and materials with little to no post-processing. In the FFF process, molten thermoplastic polymer material is extruded through a heated nozzle and deposited layer-by-layer to create the desired geometry. Polymers utilized in such FFF processes usually obtain low relative permittivity and a high loss-tangent as they are typically designed for their mechanical properties or optical appeal and not optimized for electrical performance. Notable low-loss material exceptions like high-impact polystyrene (HIPS), polypropylene (PP), and cyclo olefin copolymer (COC) have been reported in [3]. Furthermore, several works have investigated 3D printable polymer composites that are infused with high dielectric constant nano particulate ceramic material (e.g., BaTiO3) [4–6]. Polymer composites with high relative permittivity have recently also become commercially available from manufacturers like Avient or Zetamix in the form of filaments compatible with FFF machines, leading to the proliferation of FFF additive manufacturing in microwave applications. Several works have successfully utilized such high relative permittivity filaments to create various devices in the RF, microwave, and mmWave regions. One particular design approach that is receiving an increasing amount of research attention is the utilization of AM to create structures with complex periodic internal geometries in order to engineer the dielectric properties, allowing functional grading of the effective permittivity values throughout the material. This approach of controlled heterogeneity was successfully utilized to engineer a range of RF devices with exotic dielectric properties, such as flat graded index lenses [7] and wideband

* Corresponding author.
E-mail address: simon.hehenberger@dlr.de (S.P. Hehenberger).

https://doi.org/10.1016/j.materresbull.2024.112938
Received 10 November 2023; Received in revised form 28 May 2024; Accepted 4 June 2024
Available online 7 June 2024

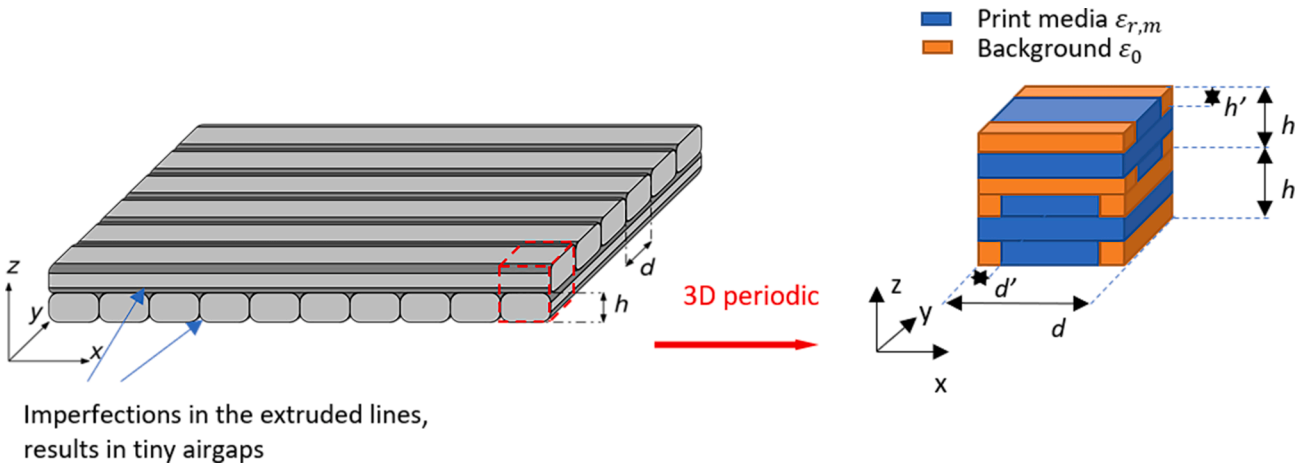

Fig. 1. FFF additive manufacturing layer buildup consists of parallel extruded lines with line width d and 90° stacked layers with layer height h. Due to printing imperfections, a 100% dense material is not possible, and rectangular inclusions with dimensions h' and d' are introduced to the unit cell to model the effects.

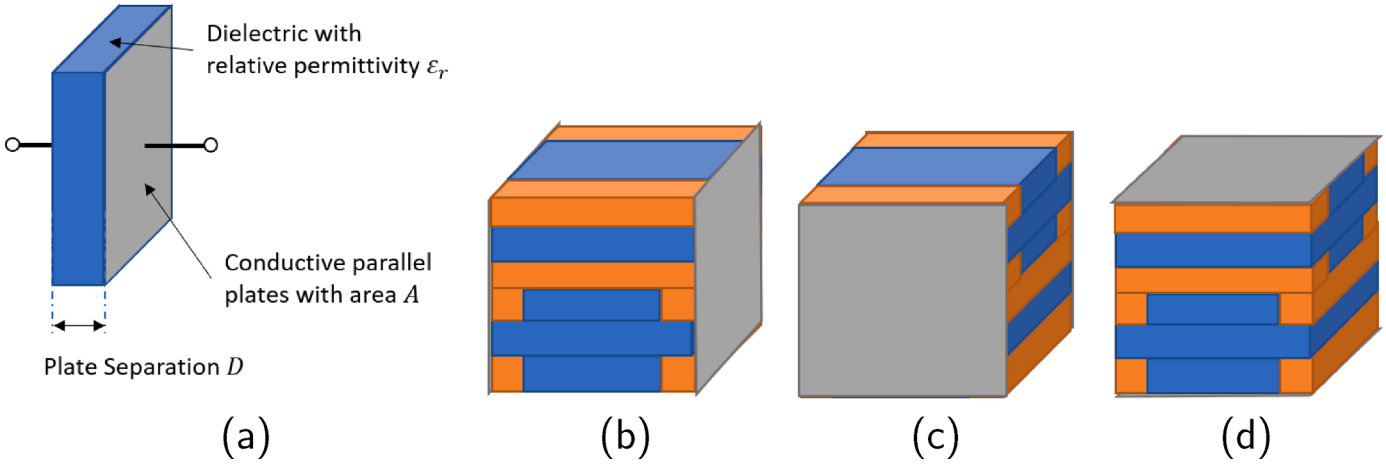

Fig. 2. Schematic representation of a parallel plate capacitor and how the principle is applied to model the effective permittivity of a complex, multi-material unit cell along its principle axis.

dielectric resonator antennas [8,9]. For more detailed information on the state of the art, latest advances, and future challenges in 3D printed antennas and metamaterials, please refer to the recently published surveys [2] and [10]. One of the significant drawbacks of FFF in general is that, due to inconsistent extrusion and air inclusions between the parallel lines and layers, it is impossible to achieve a 100 percent dense part. Furthermore, the volume of air inclusions (and, therefore, the realized relative permittivity and loss-tangent) is heavily influenced by the utilized print parameters, such as the nozzle diameter, layer height, extrusion speed, and temperatures. A recently published study considers the effect of manufacturing parameters like nozzle diameter, layer height, and print temperature on the effective permittivity of additively manufactured substrates [11]. Furthermore, the influence of design parameters of controlled heterogeneous devices like unit cell size, infill fraction, and crystal symmetry has been investigated in [12]. However, the aforementioned works study the effect of print and design parameters on the realized permittivity only in an isotropic manner. Upon closer inspection, however, the assumption of dielectric isotropy in FFF additively manufactured parts does not hold. Due to the internal structure of parallel lines and layers, the FFF fabricated material will exhibit some anisotropy in its mechanical, electrical, and thermal material parameters [13]. While mechanical, thermal, and electrical (conductivity) anisotropy of FFF printed materials is well reported in the literature, there needs to be more investigation concerning the dielectric anisotropy.

This work investigates the effect of the utilized material and manufacturing parameters like nozzle size and layer height on the permittivity tensor of FFF-manufactured materials. The rest of the article is structured as follows. In Section 2, we derive the parallel plate capacitor model for predicting the dielectric tensor of 3D printed materials and compare the results to values obtained via an electrostatic finite element method. Section 3 provides insights into the manufacturing and post-processing of samples and details the waveguide measurement setup utilized to extract the permittivity tensor of said samples. In Section 4, we will present measurement results of different samples manufactured from various materials with a wide range of permittivities and different print settings and investigate the model's applicability to predict measured permittivity tensor components.

2. Modelling

Geometries manufactured via FFF methods are generally built layer by layer with parallel extruded lines where individual layers are rotated 90 degrees with respect to each other, as indicated in Fig. 1 where x and y denote line directions and z the layer stack axis. This geometry can be modeled via a 3D periodic unit cell consisting of two stacked and 90× rotated lines of material with permittivity $\varepsilon_{r,m}$, with layer height h, and

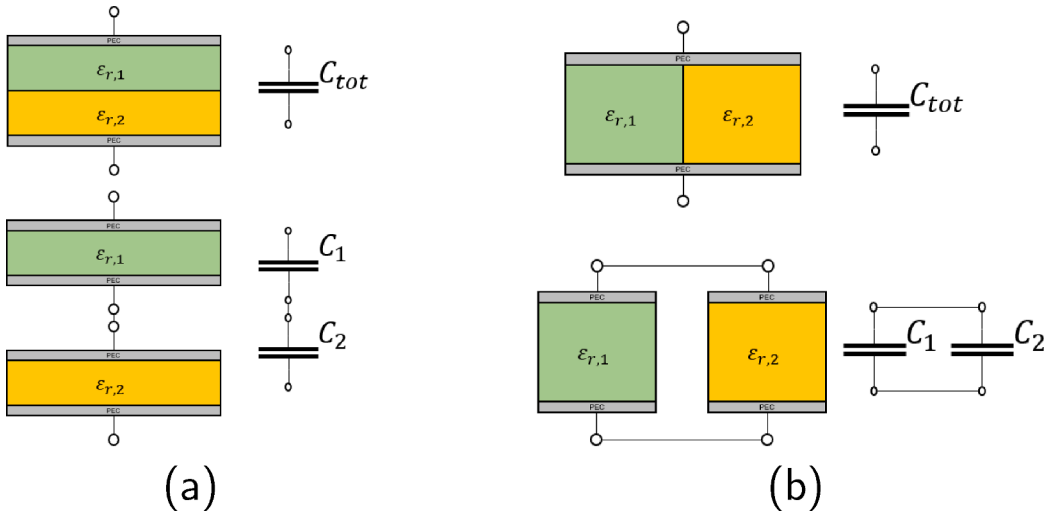

Fig. 3. Representation of the series and parallel equivalent capacitor circuits for inhomogeneous parallel plate capacitors, assuming the electric and displacement fields are perfectly perpendicular to the PEC plates throughout the dielectric material.

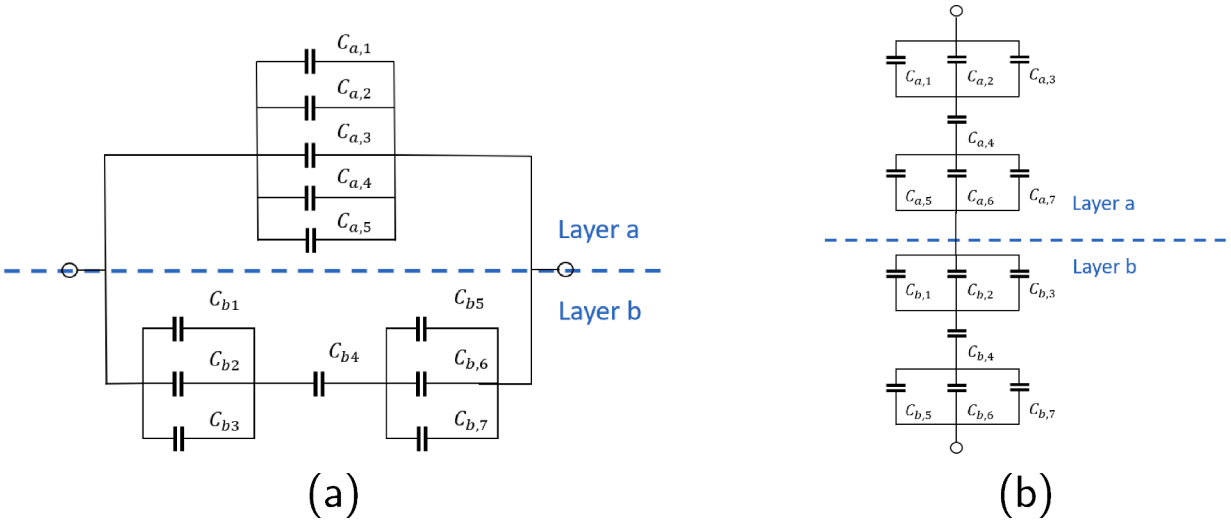

Fig. 4. Representation of the equivalent capacitor circuits modeling the anisotropy of a material manufactured with fused filament fabrication additive technologies. Each capacitor represent a homogeneous section of material in the unitcell with virtual perfectly conducting plates along (a) the x/y axis and (b) the z axis.

an extrusion width d, as depicted in Fig. 1. As mentioned above, a 100% dense part is generally impossible to achieve, and we account for this fact by introducing inclusions made from a background material $\varepsilon_{r,b}$. In this work, we consider the print material to be homogeneous and isotropic with a permittivity of $\varepsilon_{r,m}$ and the background material to be empty space $\varepsilon_{r,b} = 1$. For simplicity's sake, we consider the inclusions to be rectangular in shape with dimensions h' and d' at the edges of each extruded line. From the symmetry of the unit cell, we can already conclude that the permittivity tensor $[\boldsymbol{\varepsilon}_\mathbf{r}]$ of such a unit cell will obtain a uniaxial anisotropic shape

$$[\boldsymbol{\varepsilon}_\mathbf{r}] = \begin{bmatrix} \varepsilon_{xx} & 0 & 0 \\ 0 & \varepsilon_{yy} & 0 \\ 0 & 0 & \varepsilon_{zz} \end{bmatrix} = \begin{bmatrix} \varepsilon_O & 0 & 0 \\ 0 & \varepsilon_O & 0 \\ 0 & 0 & \varepsilon_E \end{bmatrix} \tag{1}$$

with ordinary permittivity $\varepsilon_O = \varepsilon_{xx} = \varepsilon_{yy}$ and extraordinary permittivity $\varepsilon_E = \varepsilon_{zz}$. In the following, we model the permittivity tensor of the uniaxial unit cell via an electrostatic approach based on the well-known parallel plate capacitor and compare the model to results obtained from numerical finite element simulations.

2.1. Electrostatic model based on parallel plate capacitor

The parallel plate capacitor with perfectly conducting plates of area A, separated by some dielectric with permittivity ε_r with thickness D, as depicted in Fig. 2a, is one of the simplest devices in electrostatics and its capacitance C can be easily calculated via,

$$C = \varepsilon_0 \varepsilon_r \frac{A}{D}. \tag{2}$$

We can model the effective permittivity values of the permittivity tensor's main diagonal of the unit cell depicted in Fig. 1 via assuming virtual parallel perfectly conducting plates on the individual axes, as depicted in Fig. 2b, c and d. By computing the capacitance for each of the geometries and rearranging Eq. (2), we can compute the effective capacitance of the unit cell along a given axis via

$$\varepsilon_r = \frac{CD}{\varepsilon_0 A}. \tag{3}$$

It is well known that Eq. (2) does not account for fringing fields on the edges of the plates and therefore only produces reasonably accurate results for $d \ll A$. However, in this work we assume a 2D-infinite periodic

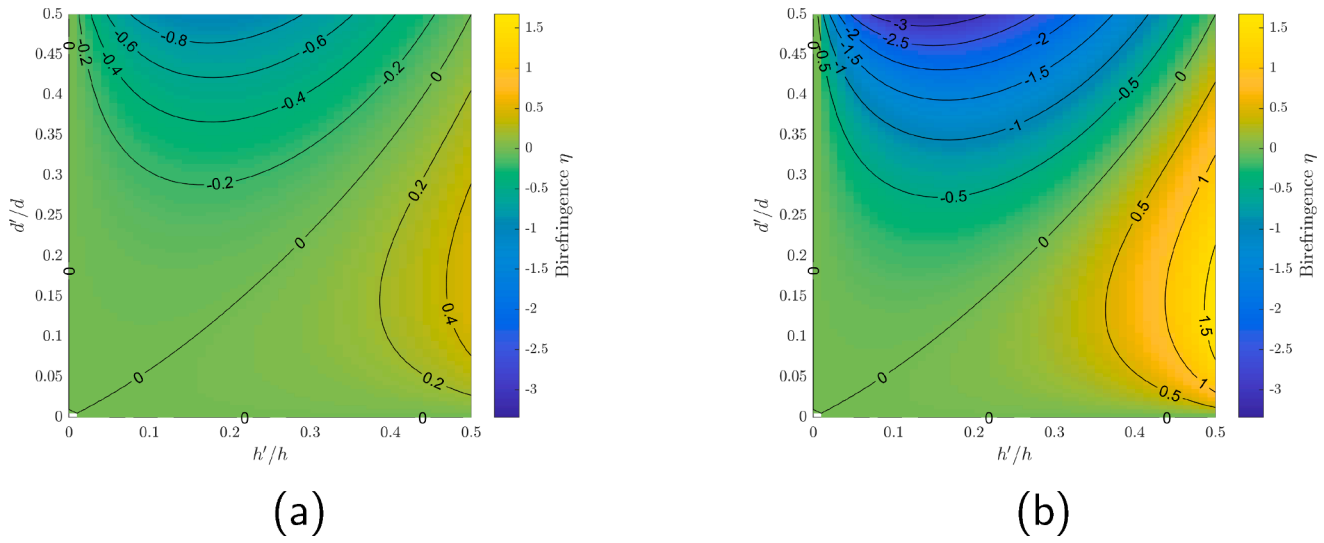

Fig. 5. Birefringence values predicted by the equivalent parallel plate capacitor model for print material relative permittivity (a) $\varepsilon_{r,m} = 4$ and (b) $\varepsilon_{r,m} = 8$ as function of h'/h and d'/d.

media between the virtual parallel PEC plates which allows to limit the investigation to the unit cell of the periodic media and neglect the influence of fringing fields on the outer plate edges. An exact solution for the capacitance of a structure with inhomogeneous dielectric requires the solution of the Laplace equation, which is difficult to obtain in a closed form for complex structured unit cells with different materials, as considered in this work. In order to obtain a closed-form solution for the permittivity tensor components, we approximate the electric field and the electric displacement field in the material to be perfectly perpendicular to the parallel plates, thus ignoring fringing fields along or between dielectric interfaces. With this assumption, we can separate the complex unit cell into an equivalent circuit of series and parallel capacitances representing the individual homogeneous material sections as depicted in Fig. 3.

This method of computing the capacitance is applied to the unit cell in Fig. 1 along its x/y and z axis below.

2.1.1. Capacitance along x/y - ordinary Axis

To compute the capacitance of the unit cell depicted in Fig. 1, we apply virtual perfectly conducting plates as depicted in Fig. 2b and c. Splitting the unit cell into equivalent capacitances representing the homogenous material sections in the unit cell along the x-axis, we obtain the equivalent circuit depicted in Fig. 4a. We can split the equivalent circuit into two individual layers, which are parallel aligned. For layer *a*, we find the capacitances

$$C_{a,1} = C_{a,2} = C_{a,3} = C_{a,4} = \varepsilon_0 \frac{d'h'}{d} \tag{4}$$

for the inclusions and

$$C_{a,5} = \varepsilon_0 \varepsilon_{r,m} \frac{dh - 4d'h'}{d} \tag{5}$$

for the material part. Since in layer *a* all homogeneous material sections are aligned parallel we can find the equivalent capacitance as

$$C_a = 4C_{a,1} + C_{a,5}. \tag{6}$$

In layer *b* we find the capacitances

$$C_{b,1} = C_{b,3} = C_{b,5} = C_{b,7} = \varepsilon_0 \frac{dh'}{d'} \tag{7}$$

and

$$C_{b,2} = C_{b,6} = \varepsilon_0 \varepsilon_{r,m} \frac{dh - 2dh'}{d'} \tag{8}$$

for the three homogeneous material sections adjacent to the virtual PEC plates. Furthermore, for the middle section we find

$$C_{b,4} = \varepsilon_0 \varepsilon_{r,m} \frac{dh}{d - 2d'}. \tag{9}$$

The capacitance of layer *b* can be expressed via

$$C_b = \left(\frac{2}{2C_{b,1} + C_{b,2}} + \frac{1}{C_{b,4}} \right)^{-1}. \tag{10}$$

Due to the parallel alignment of layer *a* and *b* the total capacitance of the unit cell along the x axis can be expressed as

$$C_x = C_a + C_b \tag{11}$$

and, as mentioned above, due to the symmetry of the unit cell,

$$C_y = C_x. \tag{12}$$

2.1.2. Capacitance along z - extraordinary axis

Investigating the capacitance of the unit cell along the z-axis, as depicted in Fig. 2 d, the equivalent capacitance circuit, representing the individual homogneous sections of the unit cell, in Fig. 4b is obtained. As done above, the equivalent circuit is split into the individual layers, which are serially aligned this time. In layer *a* we find capacitances

$$C_{a,1} = C_{a,3} = C_{a,5} = C_{a,7} = \varepsilon_0 \frac{dd'}{h'} \tag{13}$$

and

$$C_{a,2} = C_{a,6} = \varepsilon_0 \varepsilon_{r,m} \frac{d^2 - 2dd'}{h'} \tag{14}$$

for the parallel material sections adjacent to the virtual PEC plates and

$$C_{a,4} = \varepsilon_0 \varepsilon_{r,m} \frac{d^2}{h - 2h'}. \tag{15}$$

Since layers a and b are 90° shifted with respect to each other but have the same geometry they obtain equal equivalent capacitances

$$C_b = C_a. \tag{16}$$

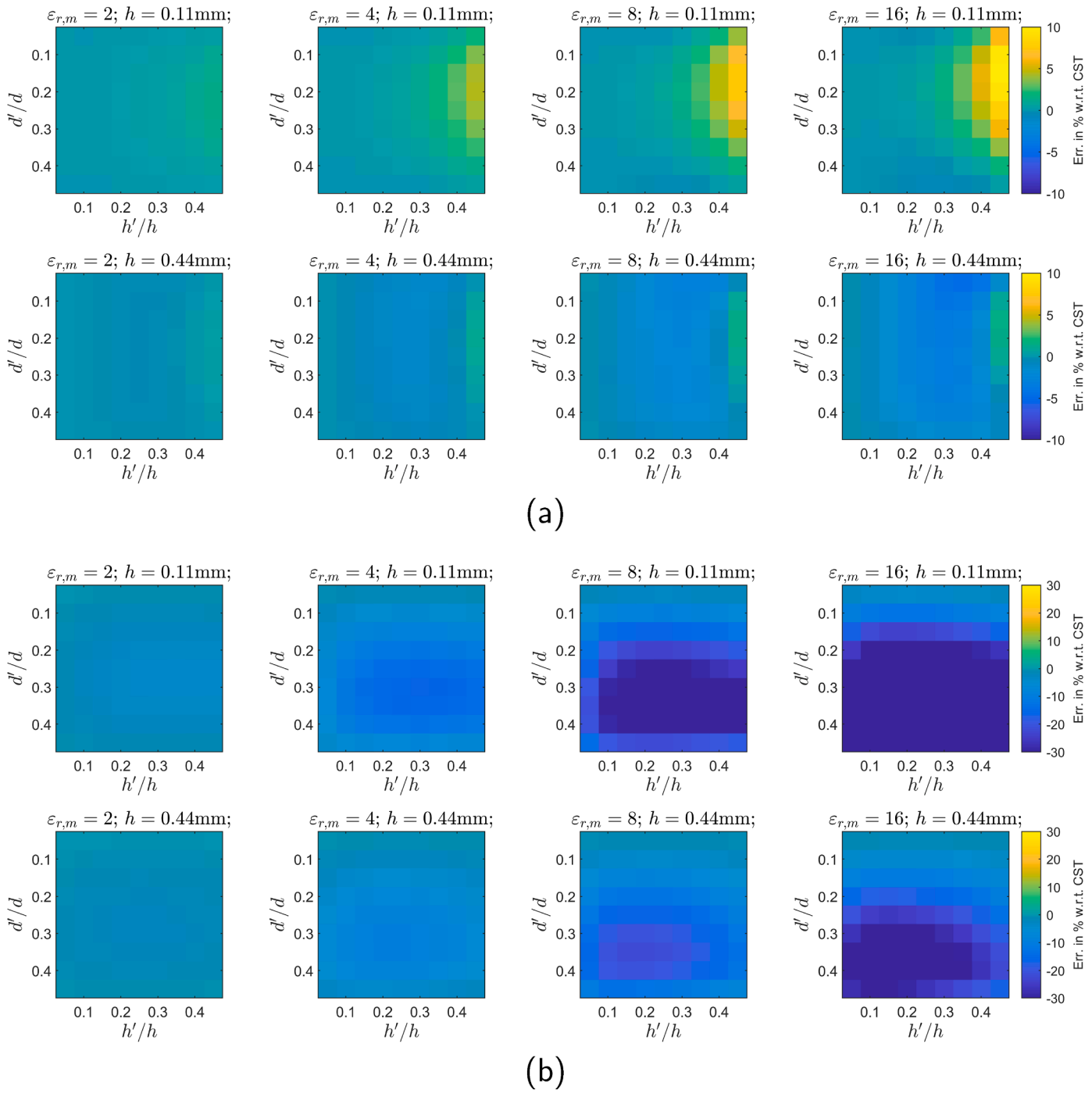

Fig. 6. Error of the (a) ordinary and (b) extraordinary permittivites as a function of inclusion dimensions h' and d' of FFF 3D printed materials predicted via a parallel plate capacitor model with respect to values obtained from an electrostatic finite element simulation for constant line width of $d = 0.55$ mm. From left to right, increasing print material permittivities $\varepsilon_{r,m}$ and from top to bottom increasing layer height h with respect to the line width d.

Table 1
Material print settings.

Material	ABS300	ABS 650	ABS1500
Nozzle temp.	225°C	235°C	285°C
Bed temp.	85°C	90°C	105°C
Max. speed	25mms^{-1}	20mms^{-1}	15mms^{-1}
Max. acceleration	400mms^{-2}	400mms^{-2}	150mms^{-2}

Finally, due to the series arrangement of the layers, the equivalent capacitance of the unit cell along the z axis can be expressed as

$$C_z = \left(\frac{2}{C_a}\right)^{-1}. \tag{17}$$

2.1.3. *Effective permittivity tensor*

With the capacitances of the unit cell computed for its principal axis above we can extract the effective permittivity tensor components for the main diagonal in (1), according to Eq. (3), as

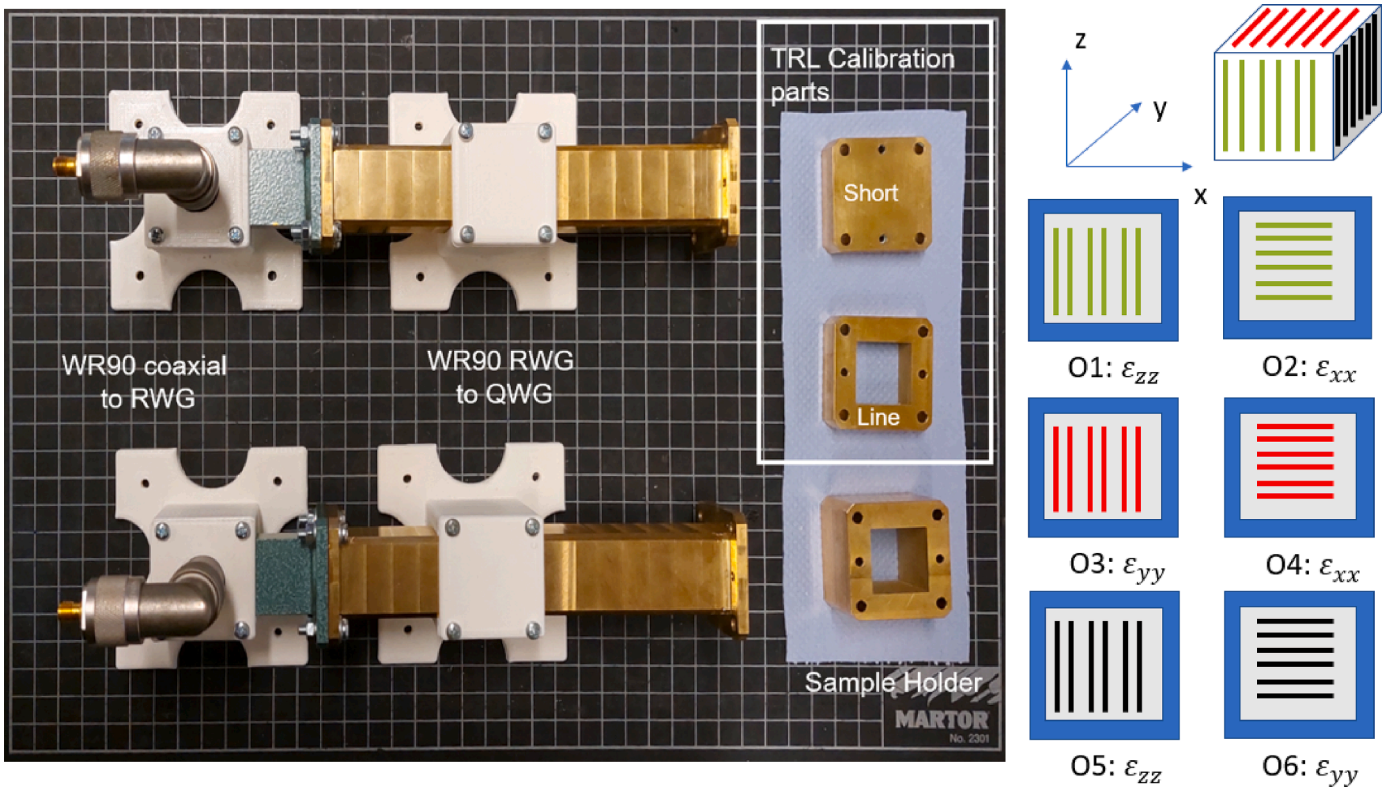

Fig. 7. Left: WR90 waveguide measurement system for anisotropic material parameter measurement with TRL calibration parts and sample holder. Right: Sample orientations and corresponding permittivity tensor components measured.

$$\varepsilon_{\mathrm{O}} = \varepsilon_{\mathrm{xx}} = \varepsilon_{\mathrm{yy}} = \frac{C_{\mathrm{x}} d}{\varepsilon_0 2hd} = -\frac{\left((8d'^2 - 4dd')\varepsilon_{\mathrm{r,m}}^2 + (8dd' - 16d'^2)\varepsilon_{\mathrm{r,m}} + (8d'^2 - 4dd')\right)h'^2}{((4dd' - 2d^2)\varepsilon_{\mathrm{r,m}} + (2d^2 + 4dd'))hh' + d^2h^2\varepsilon_{\mathrm{r,m}}} - \frac{\left(2d^2\varepsilon_{\mathrm{r,m}}^2 - 2d^2\varepsilon_{\mathrm{r,m}}\right)hh' - d^2h^2\varepsilon_{\mathrm{r,m}}^2}{((4dd' - 2d^2)\varepsilon_{\mathrm{r,m}} + (2d^2 + 4dd'))hh' + d^2h^2\varepsilon_{\mathrm{r,m}}} \tag{18}$$

and

$$\varepsilon_{\mathrm{E}} = \varepsilon_{\mathrm{zz}} = \frac{C_{\mathrm{z}} 2h}{\varepsilon_0 d^2} = -\frac{\left((2d' - d)\varepsilon_{\mathrm{r,m}}^2 - 2d'\varepsilon_{\mathrm{r,m}}\right)h}{(4d'\varepsilon_{\mathrm{r,m}} - 4d')h' + ((d - 2d')\varepsilon_{\mathrm{r,m}} + 2d')h} \tag{19}$$

While the values for h and d can be adjusted via the individual settings of the print, the values of h' and d' depend on the quality of the print setup. Uniaxial anisotropic materials can be characterized by their birefringence η, which is the difference between the extraordinay and ordinary permittivities

$$\eta = \varepsilon_{\mathrm{E}} - \varepsilon_{\mathrm{O}}. \tag{20}$$

Fig. 5 depicts the birefringence predicted from Eqs. (18) and (19) for print material relative permittivities $\varepsilon_{\mathrm{r,m}} \in \{4,\ 8\}$ as function of h'/h and d'/d. One can observe both negative and positive birefringence depending on the values of h' and d'. While we observe negative birefringence for large values of d', we observe positive birefringence for large values of h'. The larger the print material permittivity, the larger the resulting birefringence for equal h' and d'.

The investigation about the birefringence in the effective permittivity tensor of printed materials above has been carried out with respect to the real part of the tensor components. However, the model is not limited to lossless materials, and equally valid predictions can be made about the imaginary part by utilizing a complex value for the print material permittivity $\varepsilon_{\mathrm{r,m}}$ in Eqs. (19) and (18) but are omitted here for brevity sake.

2.2. Numerical investigation

In order to estimate the error due to the neglected fringing fields in the model derived above, we use the electrostatic solver in the CST software package. The unit cell depicted in Fig. 1 is implemented as a parametric model, and the capacitances along the individual principal axis are computed numerically while assuming periodic boundary conditions normal to the principal axis. The solver's mesh is refined iteratively until an energy variation threshold of below 1E-6 between consecutive iterations is reached. The permittivities from the CST simulation results are again extracted via Eq. ((3)). We compute the error with respect to the parallel plate capacitor model via

$$error_{\mathrm{O}} = \frac{\varepsilon_{\mathrm{O,CST}} - \varepsilon_{\mathrm{O}}}{\varepsilon_{\mathrm{O,CST}}} 100 \tag{21}$$

$$error_{\mathrm{E}} = \frac{\varepsilon_{\mathrm{E,CST}} - \varepsilon_{\mathrm{E}}}{\varepsilon_{\mathrm{E,CST}}} 100. \tag{22}$$

The error of the model with respect to the numerical simulations are depicted for different print material permittivities and layer heights with respect to the extrusion width in Fig. 6. One is able to observe that good predictions are achieved via the parallel plate capacitor model for low print material permittivities and that the error in the prediction of the extraordinary tensor component is always negative. Furthermore, the model error grows for small layer heights compared to the extrusion width. A similar picture is drawn for the error with respect to the imaginary part of the permittivity but omitted here for brevity sake.

3. Experimental verification

In order to test our model against experimentally obtained data,

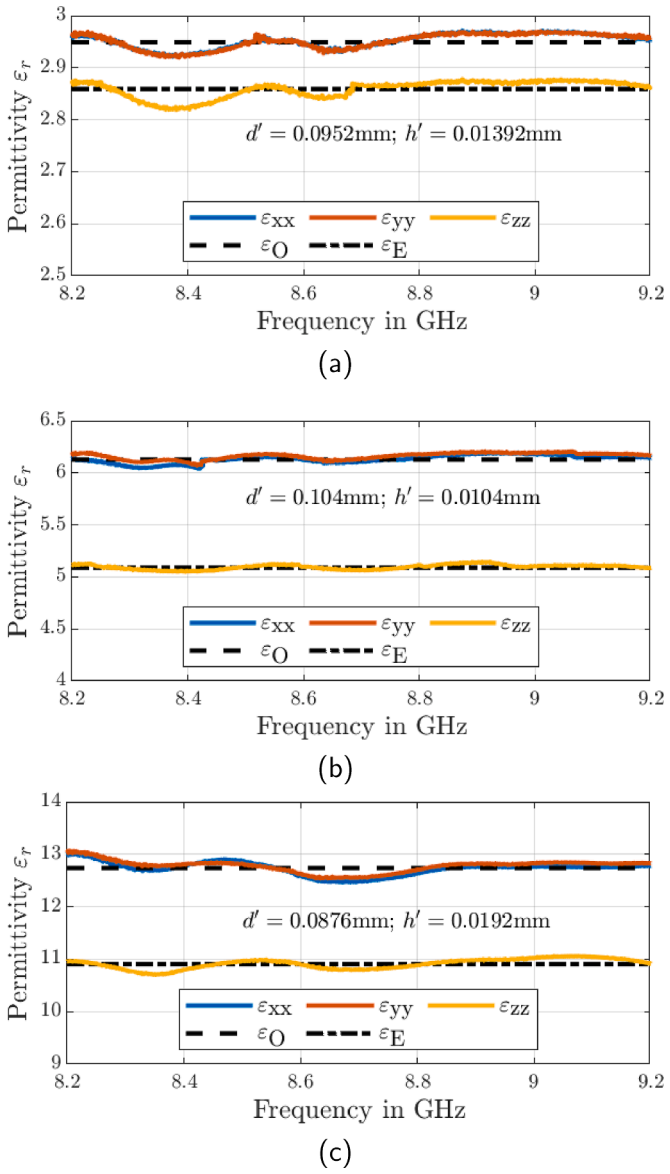

Fig. 8. Permittivity tensor main-diagonal component measurements obtained from FFF 3D printed (a) ABS300 ($\varepsilon_{r,m} = 3$), (b) ABS650 ($\varepsilon_{r,m} = 6.5$), and (c) ABS1500 ($\varepsilon_{r,m} = 15$) samples (solid lines) and comparison to predicted values (dashed lines) from equivalent parallel plate capacitor model.

several samples are manufactured from materials with a wide range of permittivities with different print settings. The utilized manufacturing equipment, materials, print settings, post-processing steps, and measurement hardware used to fabricate, prepare, and measure the individual samples are discussed below.

3.1. Printer, materials and print settings

In order to test our model against a large number of samples, three materials are selected for testing, namely the ABS300, ABS650, and ABS1500 materials from Avient (former PREPERM) with nominal permittivities of 3, 6.5 and 15 according to their respective datasheets. Samples for measurement are printed with three different nozzle sizes (0.25 mm, 0.4 mm, and 0.6 mm), as well as two different layer heights for each nozzle size. In order to present data with statistical significance, three individual samples for each material, nozzle size, and layer height combination are fabricated, resulting in 54 samples to be measured. Samples are printed with customized 3D printing hardware based on the E3D motion system with direct-drive Hemera extruders. The selected materials are based on an acrylonitrile-butadiene-styrol (ABS) copolymer matrix infused with a high dielectric constant nanoparticulate ceramic material to engineer their relative permittivity. However, the high ceramic content makes the materials abrasive, and specially hardened nozzles are required to print without wear and tear, impacting print quality during manufacturing. We utilize the commercially available "Nozzle X" made from nickel-plated tool steel to avoid issues from abrasive materials. Print settings for the individual material, nozzle size, and layer height combinations are listed in Table 1.

3.2. Measurement setup and sample preparation

Due to variations in the printing process it is desirable to extract the material permittivity tensor from a single sample. Another significant factor is the sample size required. Small samples create issues with printing tolerances and repeatability, too large samples would require tremendous amount of material and printing time. To address this issue a dedicated X-band waveguide system, depicted in Fig. 7, for anisotropic material parameter measurement requiring only a single cube shaped sample as introduced in [14] is devised. The system consists of common WR90 coaxial to waveguide transition but then utilizes a tapered waveguide section to transit from a rectangular to a quadratic aperture. This allows the measurement of a perfectly cube-shaped sample in six different orientations in the sample holder and thus enables extraction of the main diagonal components of the permittivity and permeability tensor via the Nicholson-Ross-Weir (NRW) method. As this work only deals with dielectric materials, the assumption of non-magnetic material $\mu_r = 1$ is generally imposed on the utilized NRW procedure. This leads to a more accurate and stable computation of the material under test's complex permittivity [15]. Due to the tapering of the standard WR90 rectangular waveguide to a quadratic aperture, higher-order modes exhibit a lower cut-off frequency, thus reducing the upper limit of the measurement bandwidth from 12.4 GHz to ≈ 9.2 GHz. Prior to measurement, the system is calibrated via a through-reflect-line (TRL) calibration with reference planes at the end of the quadratic tapering section.

The different nozzle size and layer height combinations utilized during manufacturing of the individual samples imply different tolerances and surface qualities which affect the quality of measurements. In order to homogenize the dimensions and surface qualities, individual samples are printed slightly bigger than required and reduced in a post-processing step to precisely match the required dimensions of the waveguide measurement system utilizing a computerized numerically controlled (CNC) milling machine.

4. Results

Measurement results for the real main-diagonal components of the permittivity tensor of individual samples of the three utilized materials are depicted in Fig. 8 as a function of frequency respectively. One is able to observe uniaxial characteristics for each of the individual samples with measured values for ε_{xx} and ε_{yy} (extruder movement directions) aligning perfectly with each other and different measured values for ε_{zz} (layer stack direction). The small oscillations of the measured permittivity values as a function of frequency can be most likely attributed to an imperfect calibration of the setup. The observed anisotropy is especially prominent for samples printed from material with high relative permittivity, as can be observed in Fig. 8 c. For a given material and print settings d and h we can extract the values of the inclusion dimensions d' and h' by performing a least-squares fit of the real measured permittivity data to the model described by Eqs. (18) and (19). The values for the inclusion dimensions d' and h' for the measurement data shown in Fig. 8a, b, and c and the corresponding predicted tensor components ε_O and ε_E are depicted in the same Figures. One is able to observe an excellent agreement between the predicted and measured

Table 2
Measurement results for all permittivity tensor components ε_{xx}, ε_{yy} and ε_{zz} for all print materials ABS300, ABS650 and ABS1500, and print settings h and d with extracted inclusion dimensions h' and d'.

Material	d in mm	h in mm	ε_{xx}	ε_{yy}	ε_{zz}	η	d' in mm	h' in mm
ABS300	0.25	0.1	$2.928 - 0.022i \pm 0.015$	$2.943 - 0.019i \pm 0.0156$	$2.845 - 0.022i \pm 0.016$	0.090 ± 0.016	0.106 ± 0.018	0.0024 ± 0.0013
ABS300	0.25	0.16	$2.901 - 0.021i \pm 0.015$	$2.915 - 0.019i \pm 0.016$	$2.841 - 0.022i \pm 0.018$	0.067 ± 0.018	0.081 ± 0.025	0.0074 ± 0.0045
ABS300	0.4	0.16	$2.846 - 0.030i \pm 0.010$	$2.863 - 0.029i \pm 0.010$	$2.791 - 0.032i \pm 0.009$	0.064 ± 0.009	0.100 ± 0.004	0.0122 ± 0.0018
ABS300	0.4	0.24	$2.834 - 0.026i \pm 0.014$	$2.879 - 0.029i \pm 0.015$	$2.786 - 0.030i \pm 0.018$	0.071 ± 0.018	0.091 ± 0.003	0.0211 ± 0.0019
ABS300	0.6	0.24	$2.928 - 0.022i \pm 0.015$	$2.931 - 0.029i \pm 0.017$	$2.824 - 0.023i \pm 0.013$	0.106 ± 0.013	0.272 ± 0.019	0.0050 ± 0.0014
ABS300	0.6	0.36	$2.913 - 0.025i \pm 0.017$	$2.902 - 0.025i \pm 0.035$	$2.850 - 0.040i \pm 0.018$	0.057 ± 0.018	0.204 ± 0.006	0.0115 ± 0.0011
ASB650	0.25	0.1	$6.043 - 0.061i \pm 0.062$	$6.082 - 0.048i \pm 0.052$	$5.047 - 0.051i \pm 0.035$	1.016 ± 0.035	0.112 ± 0.004	0.0047 ± 0.0009
ABS650	0.25	0.16	$6.002 - 0.061i \pm 0.057$	$6.035 - 0.051i \pm 0.053$	$5.100 - 0.052i \pm 0.041$	1.009 ± 0.041	0.102 ± 0.005	0.0082 ± 0.0016
ASB650	0.4	0.16	$5.993 - 0.069i \pm 0.055$	$5.855 - 0.050i \pm 0.191$	$5.021 - 0.036i \pm 0.033$	0.903 ± 0.020	0.175 ± 0.013	0.0085 ± 0.0024
ABS650	0.4	0.24	$5.927 - 0.093i \pm 0.067$	$5.926 - 0.084i \pm 0.068$	$5.033 - 0.072i \pm 0.029$	0.893 ± 0.029	0.165 ± 0.004	0.0150 ± 0.0013
ASB650	0.6	0.24	$5.916 - 0.059i \pm 0.071$	$5.975 - 0.046i \pm 0.054$	$5.134 - 0.036i \pm 0.033$	0.811 ± 0.034	0.236 ± 0.009	0.0160 ± 0.0013
ABS650	0.6	0.36	$5.862 - 0.074i \pm 0.075$	$5.917 - 0.055i \pm 0.069$	$5.153 - 0.047i \pm 0.036$	0.737 ± 0.036	0.224 ± 0.006	0.0275 ± 0.0020
ASB1500	0.25	0.1	$13.225 - 0.742i \pm 0.193$	$13.113 - 0.806i \pm 0.263$	$11.505 - 0.514i \pm 0.174$	1.664 ± 0.158	0.084 ± 0.003	0.0092 ± 0.0013
ASB1500	0.25	0.16	$12.984 - 0.696i \pm 0.184$	$12.945 - 0.709i \pm 0.216$	$11.123 - 0.506i \pm 0.161$	1.846 ± 0.154	0.084 ± 0.004	0.0166 ± 0.0021
ASB1500	0.4	0.16	$13.328 - 0.651i \pm 0.187$	$13.274 - 0.703i \pm 0.226$	$11.585 - 0.538i \pm 0.180$	1.716 ± 0.172	0.136 ± 0.001	0.0137 ± 0.0013
ASB1500	0.4	0.24	$13.066 - 0.728i \pm 0.199$	$13.096 - 0.725i \pm 0.187$	$10.976 - 0.449i \pm 0.094$	2.105 ± 0.097	0.141 ± 0.002	0.0228 ± 0.0017
ASB1500	0.6	0.24	$12.849 - 0.622i \pm 0.176$	$12.781 - 0.744i \pm 0.206$	$11.022 - 0.383i \pm 0.119$	1.793 ± 0.114	0.198 ± 0.002	0.0269 ± 0.0007
ASB1500	0.6	0.36	$12.895 - 0.629i \pm 0.150$	$12.369 - 0.713i \pm 0.203$	$10.893 - 0.383i \pm 0.109$	1.739 ± 0.100	0.206 ± 0.005	0.00382 ± 0.0038

tensor components. Detailed measurement results for all samples are listed in Table 2. Extracted values for d' and h' are visualized via bar plots in Fig. 9a and b for the ABS300 material, in Fig. 9c and d for the ABS650 material and in Fig. 9e and f for the ABS1500 material respectively with error bars indicating the standard deviation of the extracted quantities.

The imaginary part of the permittivity tensor component values reported in Table 2 generally follow the same trend as the real part with respect to the different materials and print settings. However, loss measurements in traveling wave setups, and especially in waveguide setups, are less reliable due to the limited sample thickness and the additional losses due to the finite conductivity of the waveguide itself. For this reason, the investigation in this work has been carried out with emphasis on the real part of the permittivity tensor components.

Several observations can be made from the data presented in Figs. 8 and 9, and Table 2 that support the physical validity of the model:

- Inclusion dimensions d' and h' increase with increasing nozzle diameter d
- The print layer height h seems to have a significant influence on the inclusion dimension h' but a rather negligible effect on the inclusion dimension d'
- Similar values for d' and h' are obtained for samples manufactured with different materials but the same print settings d and h
- Generally, the observed trends listed above are less clear for the measurements of samples manufactured with the ABS300 material. Due to the minuscule difference in the ordinary and extraordinary permittivities, measurement errors have a significant effect on the extracted inclusion dimensions

5. Conclusion

In this work, we provide novel insights into the dielectric anisotropy of FFF 3D printed materials. We introduce an approximate model inspired by a parallel plate capacitor to model the permittivity tensor of additively manufactured layer-by-layer geometries assuming an isotropic base material and rectangular-shaped free-space inclusions. Several assumptions are applied for the model to arrive at a closed-form expression for the permittivity tensor. In order to estimate the error of the derived model, we utilize electro-static finite element simulations and conclude that the error is within reasonable bounds for low to moderate base material permittivities. The real-world applicability of the model is studied via experimental characterization of dielectric anisotropy in 3D printed samples made from different materials with a wide range of permittivities and a variety of different print parameters. The experiments are carried out using a custom waveguide measurement setup operating in the X band, capable of extracting a material permittivity tensor from a single cube shaped sample. The experimental data is fitted to the model via a least-squares approach to extract the dimensions of the modeled rectangular-shaped inclusions. Generally, good results are achieved. However, since the dimensions of the inclusions generally depend on the quality of the print setup, it is difficult to apply the model without prior knowledge of the inclusion dimension. Nevertheless, the model can be applied to estimate the permittivity tensor for a given material and print setting combination or check the quality of a given print hardware. Based on the presented work, several open topics of interest remain for future research. Optimization of print settings or adequate post-processing techniques for a minimization of the printed material birefringence may be of interest. Furthermore, this work is limited to materials manufactured with FFF additive manufacturing processes. Similar experiments with respect to other additive manufacturing techniques are of interest to the community. Additionally, in this work we limited the investigation mostly to the real part of the permittivity tensor components due to reliability issue of characterizing losses with waveguide measurement setups. A more precise investigation of the samples in terms of their losses, for example with resonance measurement methods could provide additional insights.

CRediT authorship contribution statement

Simon P. Hehenberger: Conceptualization, Methodology, Software, Investigation, Formal analysis, Data curation, Visualization, Writing – original draft, Writing – review & editing. **Stefano Caizzone:** Validation, Supervision. **Alexander Yarovoy:** Validation, Supervision.

Declaration of competing interest

The authors declare that they have no known competing financial interests or personal relationships that could have appeared to influence the work reported in this paper.

We the undersigned declare that this manuscript is original, has not been published before and is not currently being considered for publication elsewhere. We confirm that the manuscript has been read and approved by all named authors and that there are no other persons who satisfied the criteria for authorship but are not listed. We further confirm that the order of authors listed in the manuscript has been approved by all of us. We understand that the Corresponding Author is the sole contact for the Editorial process. He/she is responsible for communicating with the other authors about progress, submissions of revisions and final approval of proofs Signed by all authors as follows.

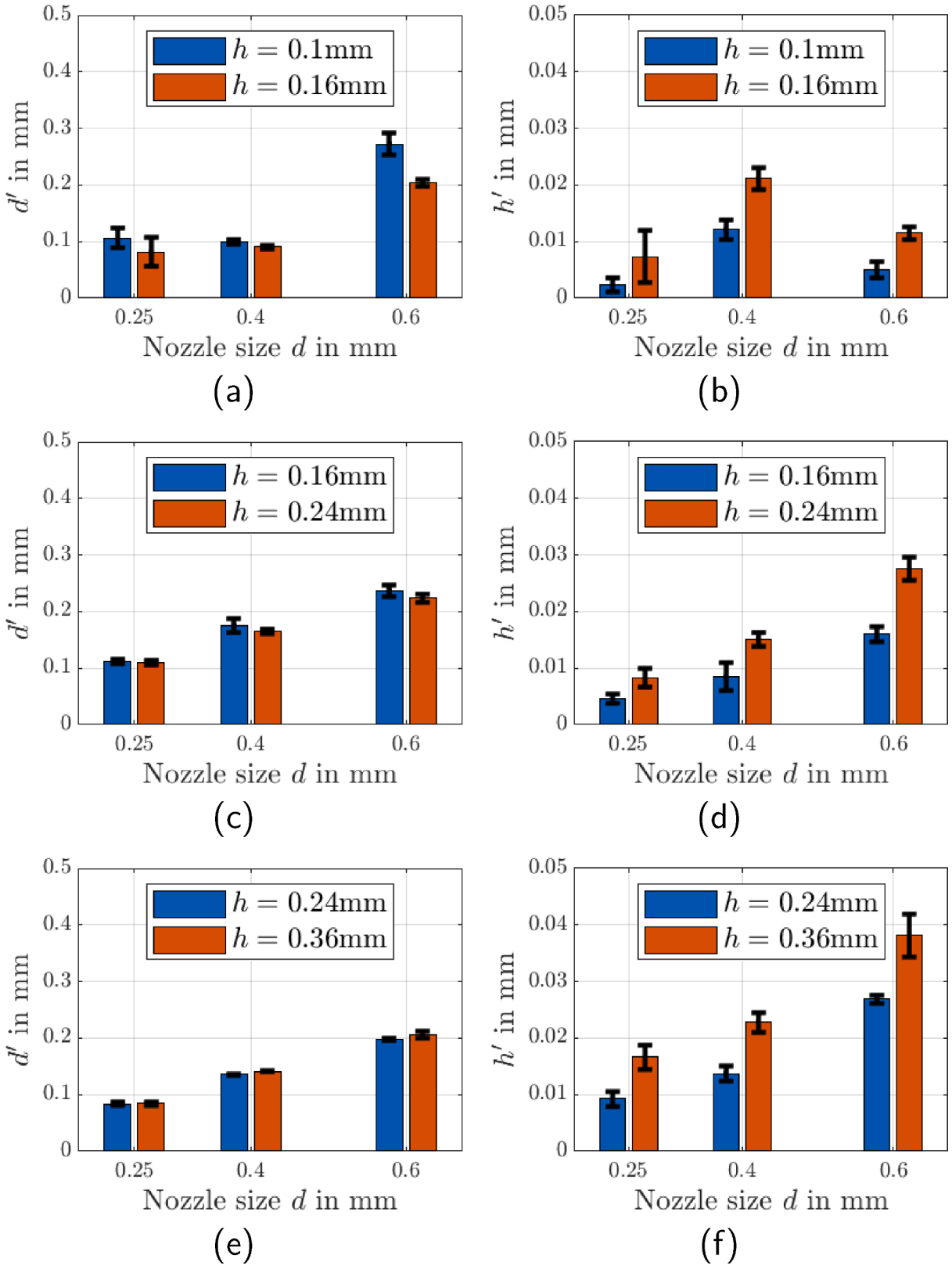

Fig. 9. Statistis of modeled rectangular inclusion dimensions h' and d' extracted from measurements of FFF 3D printed samples manufactured with extrusion width d and layer height h from (a,b) ABS300, (c,d) ABS650, and (e,g) ABS1500 with error bars indicating the standard deviation from 3 samples per material and print setting combination.

Data availability

Data will be made available on request.

References

[1] E.S. Rosker, R. Sandhu, J. Hester, M.S. Goorsky, J. Tice, Printable materials for the realization of high performance RF components: challenges and opportunities, Int. J. Antennas Propag. 2018 (2018) 1–19, https://doi.org/10.1155/2018/9359528.

[2] T. Whittaker, S. Zhang, A. Powell, C.J. Stevens, J.Y.C. Vardaxoglou, W. Whittow, 3D printing materials and techniques for antennas and metamaterials: a survey of the latest advances, IEEE Antennas Propag. Mag. 65 (3) (2023) 10–20, https://doi.org/10.1109/map.2022.3229298.

[3] C.J. Stevens, I. Spanos, A. Vallechi, J. McGhee, W. Whittow, 3d printing of functional metal and dielectric composite meta-atoms, Small 18 (10) (2022) e2105368, https://doi.org/10.1002/smll.202105368.

[4] C.K. Chiang, R. Popielarz, Polymer composites with high dielectric constant, Ferroelectrics 275 (1) (2002) 1–9, https://doi.org/10.1080/00150190214285.

[5] Z.-M. Dang, J.-K. Yuan, J.-W. Zha, T. Zhou, S.-T. Li, G.H. Hu, Fundamentals, processes and applications of high-permittivity polymer-matrix composites, Prog. Mater. Sci. 57 (4) (2012) 660–723, https://doi.org/10.1016/j.pmatsci.2011.08.001.

[6] Y. Wu, D. Isakov, P. Grant, Fabrication of composite filaments with high dielectric permittivity for fused deposition 3D printing, Materials 10 (10) (2017) 1218, https://doi.org/10.3390/ma10101218.

[7] J.W. Allen, B.I. Wu, Design and fabrication of an RF GRIN lens using 3D printing technology. Terahertz, RF, Millimeter, and Submillimeter-Wave Technology and Applications VI, 2013.San Francisco, California, USA

[8] Q. Lamotte, G. Mazingue, J. Bhatker, M. Romier, N. Capet, N. Delhote, K. Elis, Multi-permittivity 3D-printed ceramic dual-band circularly polarized dielectric resonator antenna for space applications. 2021 15th European conference on antennas and propagation (euCAP). Presented at the 2021 15th European Conference on Antennas and Propagation (EuCAP), 2021, https://doi.org/10.23919/eucap51087.2021.9411245.Dusseldorf, Germany

[9] S.P. Hehenberger, S. Caizzone, A.G. Yarovoy, Additive manufacturing of linear continuous permittivity profiles and their application to cylindrical dielectric resonator antennas, IEEE Open J. Antennas Propag. 4 (2023) 373–382, https://doi.org/10.1109/ojap.2023.3258147.

[10] Y. Wang, X. Zhang, R. Su, M. Chen, C. Shen, H. Xu, R. He, 3D printed antennas for 5G communication: Current progress and future challenges, Chin. J. Mech. Eng. Addit. Manuf. Front. 2 (1) (2023) 100065, https://doi.org/10.1016/j.cjmeam.2023.100065.

[11] A. Goulas, S. Zhang, D.A. Cadman, J. Järveläinen, V. Mylläri, W.G. Whittow, D. S. Engstrøm, The impact of 3D printing process parameters on the dielectric properties of high permittivity composites, Designs 3 (4) (2019) 50, https://doi.org/10.3390/designs3040050.

[12] S.P. Hehenberger, S. Caizzone, S. Thurner, A.G. Yarovoy, Broadband effective permittivity simulation and measurement techniques for 3-D-printed dielectric crystals, IEEE Trans. Microwave Theory Tech. 71 (10) (2023) 4161–4172, https://doi.org/10.1109/tmtt.2023.3259479.

[13] N. Zohdi, R.C. Yang, Material anisotropy in additively manufactured polymers and polymer composites: a review, Polymers 13 (19) (2021) 3368, https://doi.org/10.3390/polym13193368.

[14] A. Knisely, M. Havrilla, P. Collins, Biaxial anisotropic sample design and rectangular to square waveguide material characterization system. 2015 9th International Congress on Advanced Electromagnetic Materials in Microwaves and Optics (METAMATERIALS), 2015.

[15] J. Baker-Jarvis, E.J. Vanzura, .W.A. Kissick, Improved technique for determining complex permittivity with the transmission/reflection method, IEEE Trans. Microw. Theory Tech. 38 (8) (1990) 1096–1103, https://doi.org/10.1109/22.57336.